International Journal of Bridge Engineering (IJBE), Vol. 2, No. 3, (2014), pp. 29-58

DYNAMIC PERFORMANCE OF NOVEL BRIDGE
columns with superelastic CuAlMn shape memory alloy and ECC

Sebastian Varela[1] and M. 'Saiid' Saiidi[2]

[1,2]University of Nevada, Reno, Dept. of Civil and Environmental Engineering, United States
e-mail: svarela@unr.edu, saiidi@unr.edu

ABSTRACT: This paper presents results of experimental and analytical studies conducted on innovative bridge columns using superelastic Copper-Aluminum-Manganese (CuAlMn) SMA and ECC in the plastic hinge region. A quarter-scale column model using these advanced materials was designed and tested dynamically under near-fault ground motions on a shake table. Damage to the column model was limited to the plastic hinge region and did not compromise the column's lateral and vertical load-carrying capacity. The superelastic effect of SMA and self-confining properties of ECC allowed the column to exhibit high self-centering capabilities. A relatively simple analytical model that was implemented in OpenSees was able to match some of the key experimental results with good precision. Experimental and analytical results suggested that CuAlMn SMA and ECC used in the plastic hinge region of bridge columns in areas of high seismicity could be an alternative to keep bridges functional after strong earthquakes.

KEYWORDS: Bridge, ECC, Near Fault, Shape Memory Alloys, Shake Table

1 INTRODUCTION

Reinforced concrete bridges are critical links in any major ground transportation network and therefore in the event of failing after a strong earthquake they could cripple the entire transportation system. Direct monetary losses associated with repair or replacement of bridge structures along with indirect losses related to business disruption arising from traffic delays and detours can greatly affect the economy of a region. In addition, it is precisely after an earthquake when bridge structures are needed the most, allowing fire trucks and ambulances to respond in a timely manner and providing easy passage to crews and equipment for disaster relief. Failure in bridge systems during previous events such as the January 17, 1994 Northridge, California earthquake in the United States and the January 17, 1995 Hyogoken-Nanbu (Kobe) earthquake in Japan illustrate the need for bridges to stay functional after strong ground motion events. During the Northridge earthquake, 11 overpasses located on some of the busiest freeways in Los Angeles and the San Fernando Valley collapsed, massively

disrupting traffic for more than a month after the earthquake [1]. On the other hand, collapse of the Hanshin expressway during the 1995 Kobe earthquake affected considerably traffic in the Osaka-Kobe area, requiring more than 20 km of roadway to be demolished after complete collapse of single-column reinforced concrete piers and the entire superstructure occurred [2], [3].

Modern seismic design guidelines for standard RC bridge columns rely on the use of special reinforcement detailing rules and requirements for minimum ductility capacity of structural members to ensure plastic behavior and energy dissipation will take place during strong earthquakes. Although these guidelines result in structures having lower initial cost in comparison to a structure that is designed to behave elastically, they do not specifically address the functionality of the bridge as they are aimed mainly to minimize damage under moderate earthquake ground motions, and to prevent collapse under rare earthquakes resulting in high levels of ground shaking [4]. Consequently, under the design event the bridge is very likely to suffer significant damage and disruption to service, and may require partial or complete replacement, thereby increasing costs in the long term.

One possible strategy to mitigate damage to reinforced concrete bridge columns in regions of high seismicity is to make use of advanced materials that are able to accommodate large earthquake displacement demands without undergoing the typical severe damage expected from conventional steel-reinforced concrete members. Two of such advanced materials are Engineered Cementitious Composite (ECC) and superelastic shape memory alloys (SMAs). ECC is a grout-like material that consists of fine aggregates, Portland cement, special admixtures, and Polyvinyl Alcohol (PVA) fibers that give it superior ductility in tension and compression. One of the most important features of ECC for seismic applications is its ability to resist large compressive strains without completely losing its capacity. The fibers inside ECC act as a self-confinement mechanism, preventing the material from spalling even in the absence of transverse reinforcement [5], contrary to the behavior exhibited by conventional concrete with comparable compressive strength.

SMAs are materials that have the unique ability to undergo large deformations and recover their shape either through heating (shape memory effect) or upon stress removal (superelastic effect) [6]. Only a handful of studies assessing the earthquake performance of bridge columns using these advanced materials have been conducted. Saiidi and Wang [7] tested two quarter-scale, steel spiral reinforced concrete columns having superelastic Nickel-Titanium (NiTi) SMA longitudinal reinforcing bars in the plastic hinge region. After testing the first column model under a series of earthquake motions, the concrete in the plastic hinge region was repaired using ECC and the column was retested. It was

concluded that the flag-shaped hysteretic stress-strain of SMA leads to very small residual displacements in the columns and that repair with ECC was successful as the column only exhibited minor damage even under high-amplitude motions. Saiidi et al. [8] tested three, one-fifth scale columns under reversed slow cyclic loading. One of the models was a control conventional reinforced-concrete specimen, while the other two were both reinforced with NiTi SMA in the plastic hinge region, one using concrete and the other one using ECC. It was concluded that residual displacements in columns with SMA were considerably less than those of the conventionally reinforced column, but that ECC was needed to accommodate the large strain capacity of SMA and to reduce the extent of damage in the plastic hinge. The potential of using SMA and ECC in order to keep a bridge functional after an earthquake was also studied by Cruz-Noguez and Saiidi [9], who performed shake table tests on a large-scale 4-span bridge model. They found that the bent using SMA and ECC exhibited higher ductility than its conventional RC counterpart, in addition to providing higher self-centering and displaying lesser extent of apparent damage.

The vast majority of previous research on SMA for seismic applications involved the use of NiTi, which, despite having excellent superelastic properties, can be expensive in the practice due to the high cost of Titanium, an absence of established bridge engineering market, and because NiTi is hard to machine. A recently-developed Copper-Aluminum-Manganese superelastic SMA ([10], [11], [12], [13]) has been reported to have comparable superelastic properties to most NiTi SMAs at only a fraction of the cost due to relatively lower cost of Copper, lower production cost, and easier machinability. These studies however, have been focused mainly on the use of CuAlMn SMA wires for small-scale structural models. Larger bars of up to 0.63 in. (16 mm) in diameter have been used only for coupon tests [14]. Building on existing knowledge and as part of a project funded by the U.S. National Science Foundation, a quarter-scale Cast-In-Place reinforced concrete column model using superelastic CuAlMn SMA and ECC in the plastic hinge region was designed, constructed, and tested dynamically on a shake table. To the authors' knowledge, this is the first time CuAlMn SMA has been used and tested on a seismic bridge application at this scale. Furthermore, testing of any type of SMA-reinforced member under near-fault earthquake motions is unprecedented. The main objective of this study was to experimentally evaluate the earthquake performance of this innovative bridge column model detailed according to modern seismic design requirements. After testing the column model, an analytical study was conducted that will allow generalizing the experimental results in upcoming work. Future studies will evaluate the feasibility of using CuAlMn SMA for concrete bridge columns and identifying its possible advantages and shortcomings.

2 EXPERIMENTAL STUDIES

2.1 Model description

The quarter-scale column model was detailed according to the 2011 AASHTO Guide Specifications for LRFD Seismic Bridge design for conventional reinforced concrete bridge columns [4]. The column footing and head were made of conventional reinforced concrete and were designed to stay elastic throughout the testing. The model was designed to be tested in a cantilevered, single-curvature configuration. Since there was no test data available for conventional columns with the same dimensions subjected to near-fault motions, the longitudinal and transverse steel in the column were proportioned to be representative of those for circular bridge columns in the practice. ECC and CuAlMn SMA were used in the plastic hinge region at the lower part of the column, as shown in *Fig. 1*. SMA use was limited to the plastic hinge only because using it along the entire column height would be unnecessary and expensive. The SMA lengths above and below the footing were 10 in. (254 mm) and 2 in. (50.8 mm), respectively, and were based on an estimated plastic hinge length of about 7 in. (177.8 mm). ECC extended 21 in. (533.4 mm) or 1.5 times the column diameter above the footing level, and was placed inside the footing using a squared blockout 4 in. (101.6 mm) deep having 22 in. (558.8 mm) long sides. These dimensions were chosen to provide better continuity in the column-footing interface. Typical sections through the plastic hinge region and the rest of the column, as well as a detail of the plastic hinge are shown in *Fig. 2*.

SMA bars were connected to the longitudinal mild steel reinforcement using 2-1/8 in. (54 mm) long, 9/16-18 threaded rod coupling nuts. The engagement length inside each coupler was approximately 1 in. (25.4 mm). Use of larger #5 Grade 60 (specified yield strength of 60 ksi (420 MPa)) mild steel reinforcing bars connected to the SMA ends guaranteed yielding inside the plastic hinge region and minimal or no yielding in the mild steel outside the plastic hinge. A target axial load index (ALI) -defined as the ratio of the applied axial load to the product of the gross cross-sectional area and the specified concrete compressive strength - of about 7% was selected, as this is within typical ALIs for RC bridge columns. Table 1 summarizes the main properties of the column model. An aspect ratio (height/diameter) of around 4.5 was selected to ensure the behavior of the model would be flexure-dominated.

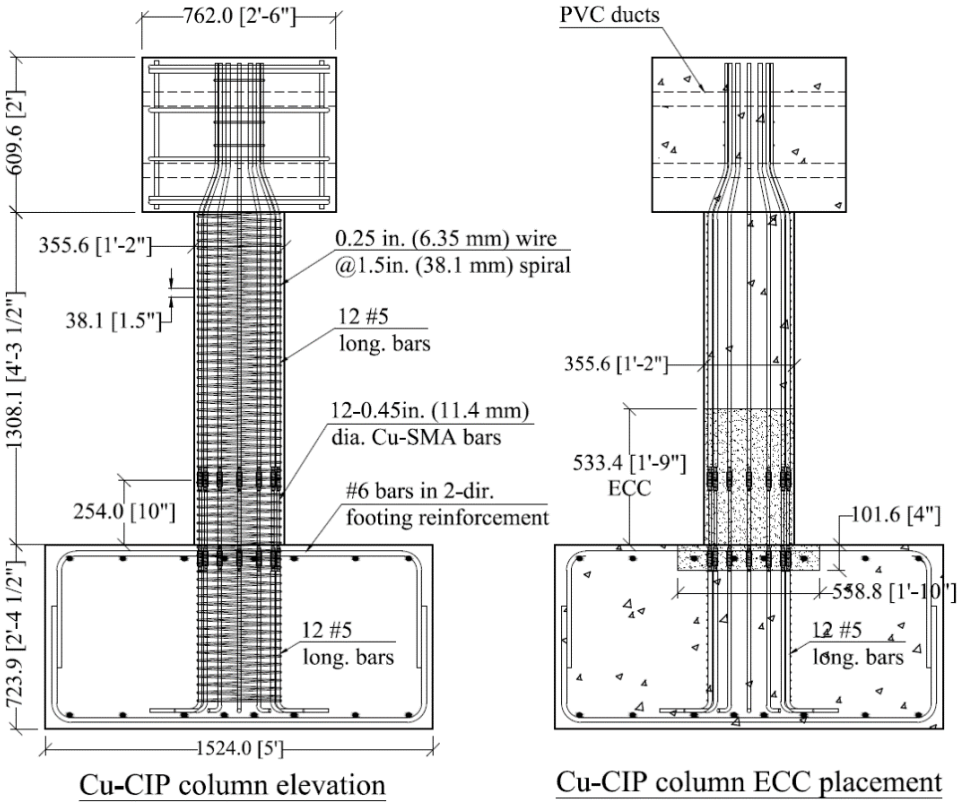

Figure 1. General column dimensions and placement of ECC in the plastic hinge region.

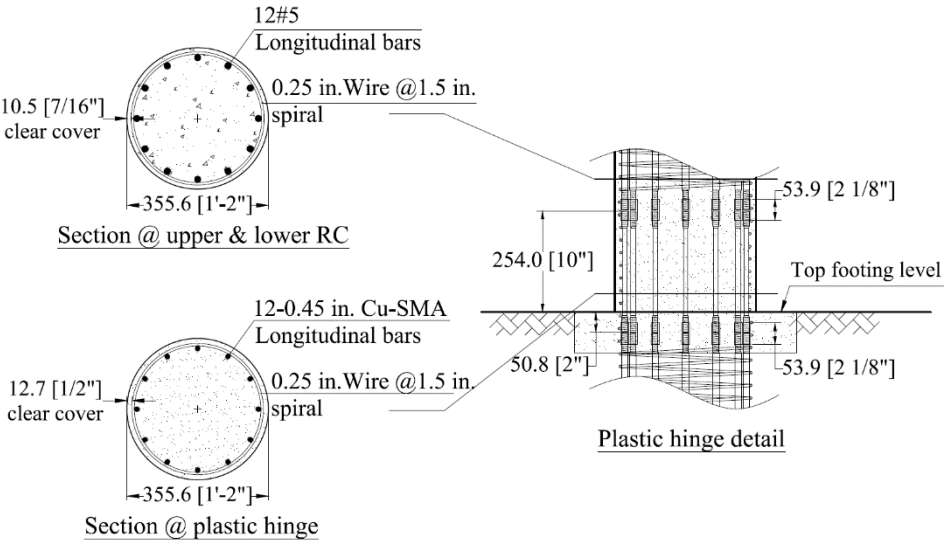

Figure 2. Typical transverse sections and plastic hinge detail.

*Table 1.*Column model properties.

Column Height, in. (mm)[a]	Diameter, in. (mm)	Long. SMA reinf. ratio (%)	Transverse Reinf.ratio (%)	Aspect ratio (Height/Dia.)	Axial Load, kips (kN)	Axial Load Index (%)[b]
63.5 (1612.9)	14 (355.6)	1.24	1.03	4.5	60 (266.9)	6.8

Notes:
[a] Column height is measured from the top of the footing to the center of the loading head.
[b] Actual ALI based on measured ECC compressive strength.

2.2 Materials

2.2.1 Copper-Based SMA

Round, superelastic CuAlMn SMA bars having a material composition with $Cu_{71.6}Al_{17}Mn_{11.4}$ were produced by Furukawa Techno Material Co., Ltd. (Hiratsuka, Kanagawa-Japan) and were then machined according to the dog-bone shape shown in *Fig. 3*. A reduced section in the middle portion of the bars and fine threads at the ends were adopted in order to avoid failure of the reduced root section at the threaded zone during testing.

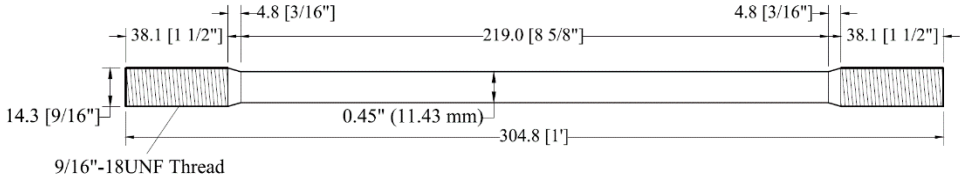

Figure 3. Machined shape of CuAlMn SMA bars.

Mechanical training on SMAs is necessary to eliminate small residual strains existing within the superelastic range of the material and to stabilize its mechanical properties. Training was performed by subjecting each SMA bar to 3 consecutive slow triangular cycles of 2% tensile strain and was conducted for all 12 SMA bars that were used in the column model as well as to an additional bar that was tested up to rupture. This procedure was crucial for the present study, as untrained SMA bars could have caused unwanted residual drifts in the column even for low testing amplitudes.

Fig. 4 and *Fig. 5* show the testing protocol and results from tensile testing of a sample CuAlMn SMA bar up to rupture, respectively. As seen in *Fig. 4*, the sample was tested first under slow cyclic loading up to a maximum strain of 8.35%, then taken back to zero stress and then finally pulled continuously to rupture. The stress-strain behavior shown in *Fig. 5* displays the typical flag-shaped hysteresis observed for superelastic SMAs, with a much narrower flag height defined by factor β, which is equal to the ratio of forward to reverse transformation stress (upper to lower yield plateaus) that was estimated at 0.20. The hysteretic parameters for the sample SMA bar are summarized in Table 2.

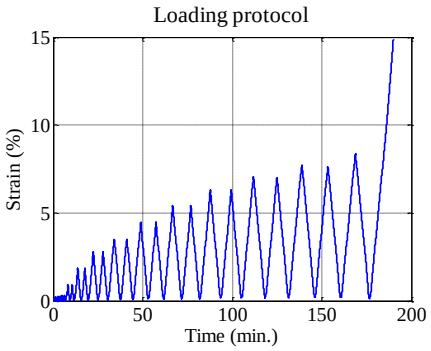

*Figure 4.*Testing protocol for the SMA bar.

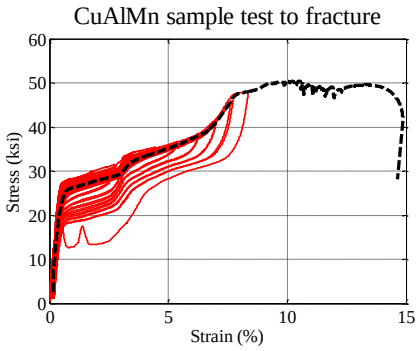

*Figure 5.*Hysteretic tensile behavior of a sample 0.45 in. (11.43 mm) CuAlMn SMA bar.

*Table 2.*Summary of measured hysteretic parameters on a sample CuAlMn SMA bar.

Parameter name	Symbol	Value
Yield (forward transf.) stress	f_y, ksi [MPa]	24 [168]
Ultimate stress	f_u, ksi [MPa]	50 [350]
Elastic modulus	k_1, ksi [GPa]	4500 [31.5]
Post-yield modulus	k_2, ksi [GPa]	280 [19.6]
Ratio of forward to reverse transformation stress	β	0.20
Superelastic strain	ε_r (%)	7
Rupture strain	ε_u (%)	14

2.2.2 ECC

Strain-hardening ECC was provided by FiberMatrix Inc. (Sparks, NV) and was

tailored to have a specified compressive strength of 6.0 ksi (42 MPa) at 28 days. A dry batch consisting of Nevada Type I/II Portland cement, Jim Bridger Class F fly ash, avg. 60# fine sand, avg. 90# silica powder, Kuraray Kuralon™RECS15 PVA fibers at a volumetric ratio of 2%, and BASF™ polycarboxylate ether or Fritz-Pak™ No. 7 superplasticizers was delivered to the construction site and mixed with water using an electrical mortar mixer. The ingredient proportions by weight are shown in Table 3.Results of compressive tests on 4 in. x 8 in. (101.6 mm x 203.2 mm) 56-day old ECC cylinder samples are shown in *Fig. 6*. The average results for the unconfined strength and strain at the maximum strength at 56 days were 5.6 ksi (39.2 MPa) and 0.0036, respectively. Although technical limitations on the compressometer that was used during testing of these cylinders only allowed measurements up to a strain of 0.015 to be taken, the ultimate unconfined strain capacity of ECC is believed to be at least 0.02. This is approximately 6 times the spalling strain of unconfined conventional concrete. The average ECC compressive strength measured at 7 and 28 days of age were 3.3 ksi (23.1 MPa) and 4.7 ksi (32.9 MPa) respectively, while the average strength on the column test day (189 days) was 7.7 ksi (54 MPa).

*Table 3.*ECC mix proportions by weight.

Cement	Water	Fly Ash	Sand (#60)	Silica powder (#90)	SP/VMA	PVA fiber by Volume
1	0.59	0.85	0.67	0.15	0.002	0.02

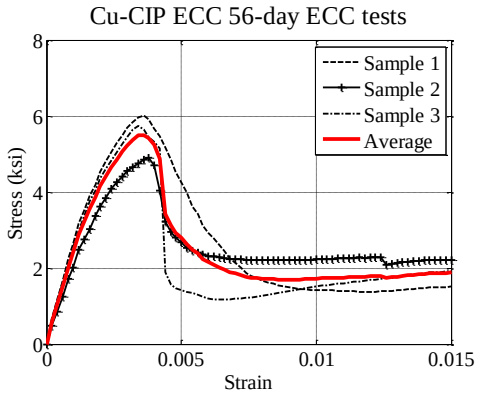

*Figure 6.*Compressive stress-strain behavior of 56 days old unconfined ECC cylinder samples.

2.2.3 Concrete

Normal-weight concrete with a specified compressive strength of 5.0 ksi (35 MPa) at 28 days and a maximum aggregate size of 3/8 in. (9.525 mm) was provided by CEMEX and was used outside the plastic hinge (footing and top of the column). The measured compressive strength of the concrete in the footing and top of the column on the day of the column tests was 5.5 ksi (38.5 MPa) and 6.5 ksi (45.5 MPa), respectively.

2.2.4 Steel reinforcing bars and spiral wire

ASTM A-615 Grade 60 mild steel reinforcing bars were used throughout the column except for the transverse reinforcement spiral. Tensile tests on 4 samples of #5 Gr. 60 bars that were used as longitudinal reinforcement in the column provided average yield and ultimate strengths of 73.5 ksi (514.5 MPa) and 105.2 ksi (736.4 MPa), respectively. The smooth spiral wire of 0.25 in. (6.35 mm) in diameter had average yield and ultimate strengths of 50 ksi (350 MPa) and 60 ksi (420 MPa), respectively.

2.3 Model construction

The column rebar cage with SMA bars attached was secured to the footing, which was built first. A square blockout was used to provide the space for ECC inside the footing (*Fig. 7*). The concrete surface inside the blockout was left intentionally rough after casting to enhance bond with ECC (*Fig. 8*).

*Figure 7.*CuAlMn SMA bars in the plastic hinge and blockout for ECC.

*Figure 8.*Completed concrete in the footing.

After casting the footing concrete, a round Sonotube® cardboard form was used to provide the shape for the concrete and ECC in the column. ECC was cast from the top and vibrated from outside the form using a rotary hammer pressed against the Sonotube. A few days after and once the ECC had hardened (Fig. 9), formwork was built for the upper column head and concrete was placed from the top using a metal round-gate concrete bucket. No special provisions for

curing were taken since concrete and ECC were cast on late September and early October, when the average ambient temperature in Reno, NV is approximately 66ºF (19ºC). The completed column is shown in *Fig. 10*.

*Figure 9.*Completed ECC.

*Figure 10.*Completed column.

2.4 Test setup and instrumentation

The column model was tested on a shake table at the new Earthquake Engineering Laboratory at the University of Nevada, Reno, as shown in *Fig. 11*. Ground motions were uniaxial and were applied along the N-S direction of the laboratory, as depicted in *Fig. 11*. The footing was placed over a 1.5 in. (38.1 mm) thick grout pad and was rigidly attached to the shake table using pre-tensioned high-strength all thread bolts. A mass-rig consisting of a steel frame having vertical load-carrying capacity but negligible lateral stiffness was connected to the column head and was used to apply inertial mass to the model in a safe manner. A rigid link having swiveled ends transferred the inertial forces from the mass-rig to the column model. A load cell that was placed in between the link and the head of the columns allowed measuring the resisting force of the model directly.

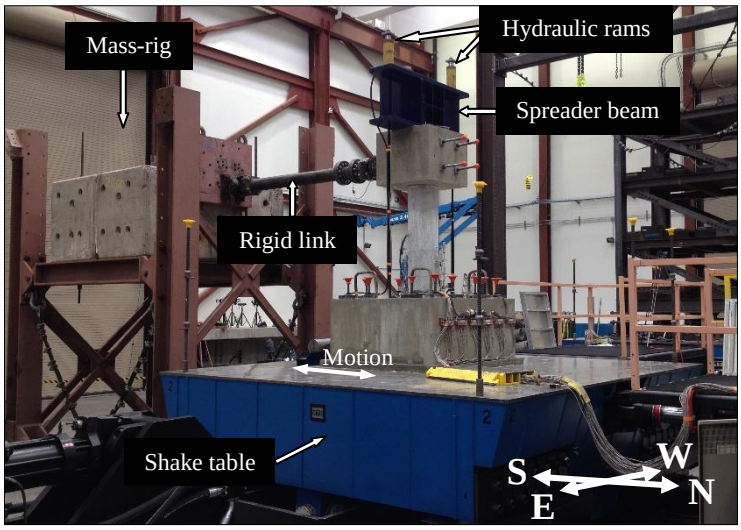

*Figure 11.*Shake table test setup.

Several other instruments were used to capture the response of the column including string potentiometers, displacement transducers, accelerometers, strain gauges, and video cameras. Axial load was applied to the model using pressure-controlled hydraulic rams placed over a stiff spreader steel beam on top of the column head. Each ram provided 30 kips (133.4 kN) axial load for a total applied load of 60 kips (266.9 kN). In order to provide the correct inertial mass to the model, the axial load was matched using two-20 kip (89 kN) concrete blocks placed on the mass-rig and 20 additional kips from the mass-rig's inertial weight. Data from the different instrument channels was collected using a data-acquisition system at a sampling rate of 256 Hz.

2.5 Pre-test analyses for selection of ground motion and testing protocol

Extensive pre-test analytical studies were conducted in order to determine the ground motion and loading protocol. A near-fault record characterized by a short duration-high amplitude ground velocity pulse was selected to maximize the tendency for high residual lateral displacements, as has been observed for conventional RC specimens subjected to near-fault motions [15]. In addition, the number of cycles causing large strains in the SMA bars was taken into account at the time of selecting the ground motion, as the low cycle fatigue characteristics of CuAlMn SMA were unknown. Based on the analytical results under several different ground motions, the Rinaldi Receiving Station (RRS 228) record of the 1-17-1994 Northridge, California earthquake was chosen. The time axis in the acceleration record was multiplied by a factor of $1/\sqrt{4}$ to account for geometric scaling of the model, which was 1/4. The unscaled

ground acceleration and velocity histories for the selected motion are shown in *Fig. 12*.

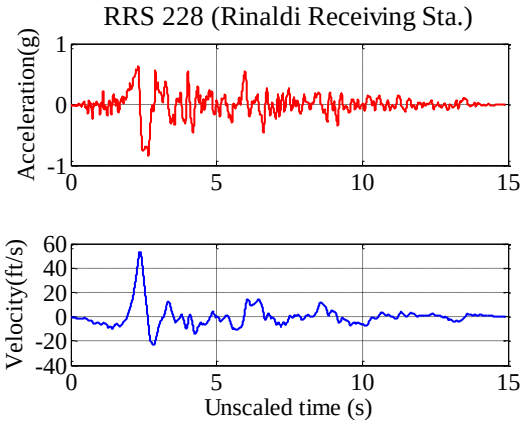

*Figure 12.*Unscaled acceleration and velocity histories for the selected RRS228 (Rinaldi Receiving Station) Northridge Earthquake ground motion.

After choosing a location for a hypothetical bridge in a region of high seismic hazard (Reno, NV) having a site class D (stiff soil) and an assumed Seismic Design Category (SDC) type D, a design spectrum was determined based on the design maps given by the 2009 AASHTO Guide Specifications for LRFD Seismic Bridge Design. The design spectral acceleration, referred to as the 'design' ground motion (100% x DE), was then determined based on the vibration period of a cantilevered column with a seismic weight of 60 kips (266.9 kN) and an effective flexural stiffness $(EI)_{eff}$ of 77.46×10^4 kips-in^2 (2.22×10^3 kN-m^2).This effective stiffness was taken as the slope of the elastic portion of an elasto-plastic idealization of the moment-curvature curve for the plastic hinge section of the column. The amplitudes for the testing protocol were then determined based on the scaling factors needed for the Rinaldi record to reach certain percentages of the 'design' earthquake spectral ordinate. Analytical results showed that a protocol having runs of 25%, 50%, 100%, 150%, 200% and possibly>=300% the design earthquake would provide a good insight of the full hysteretic behavior of the model up to approximately 7 to 8% drift. In between earthquake runs the column model was inspected thoroughly for signs of distress, and white noise motions were applied in order to monitor changes in the fundamental period due to progression of any damage to the column.

3 TEST RESULTS AND DISCUSSION

3.1 Achieved versus target ground motions

Characteristics of the runs applied to the column model are summarized in

Table 4, where the target and achieved scaling factors and peak ground acceleration (PGA) for each run are listed. Based on the PGA, it can be seen that achieved runs above Run 3 (100% x DE) were somewhat larger and hence more demanding that the target. However, evaluation of the 5%-damped achieved and response spectra for each run (*Fig. 13*) reveals a very good match between the two and provides reliance in the shake table's control system ability to accurately reproduce the frequency content and amplitudes of the selected ground motions. Since a Butterworth filter with cutoff frequencies of 0.05 Hz and 50 Hz was applied to the RRS 228 ground motion for control purposes, the shape of the target spectra in *Fig. 13* differs slightly from that of the original unfiltered ground motion.

*Table 4.*Summary of target and achieved ground motions.

	Target			Achieved		
Run #	Motion PGA (g)	x Rinaldi (RRS 228)	x DE	Motion PGA (g)	x Rinaldi (RRS 228)	x DE
1	0.073	0.087	25%	0.078	0.094	27%
2	0.145	0.173	50%	0.167	0.199	57%
3	0.290	0.346	100%	0.352	0.420	121%
4	0.435	0.520	150%	0.543	0.649	187%
5	0.580	0.693	200%	0.735	0.878	254%
6	0.871	1.039	300%	1.134	1.353	391%
7	1.016	1.212	350%	1.314	1.569	453%

3.2 Extent of apparent damage

As seen in *Fig. 12*, the applied ground motion was asymmetrical and was oriented such that the model experienced a larger relative displacement pulse directed towards the south (see *Fig. 11*). This direction was referred to as the 'dominant' direction and caused predominantly tension in the bars closer to the north and compression in those closer to the south.

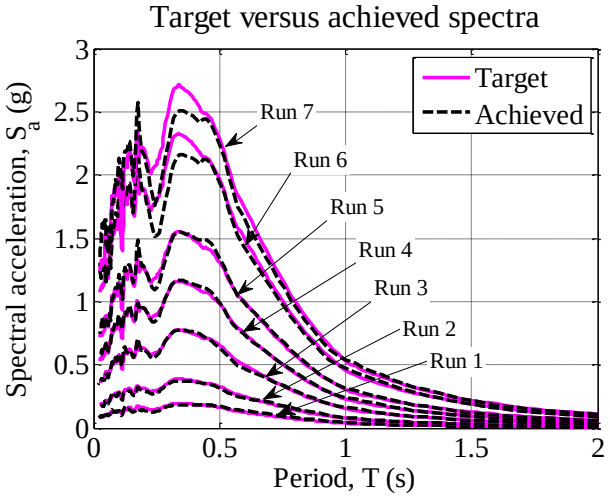

*Figure 13.*Target versus achieved shake table acceleration response spectra for each run.

As stated before, the column model was inspected after each earthquake run for signs of distress such as cracking and spalling of concrete and ECC. A white wash coating made of mixed water and lime was applied to the column and footing surfaces before testing to allow easy identification and marking of cracks. The first flexural cracks appeared on the bottom quarter of the plastic hinge after Run 2 (*Fig. 14*), and were consistent with tension occurring in the north and compression in the south. A single larger tensile crack with a triangular shape appeared on the north side after Run 2 and was joined progressively through subsequent runs by multiple smaller cracks. Flaking of the ECC was observed at the ends of this larger crack in the footing after Runs 6 and 7. Minor localized compressive failure of ECC occurred at the column-footing interface on the south side starting from Run 2, but no apparent loose chunks of ECC were noted until after Run 7, when a piece of ECC cover on the south delaminated. No spiral or SMA bars were visible even after this piece had been removed. The self-confining effect of the fibers inside the ECC was evident since the crack causing this piece to come loose after Run 7 appears to have formed starting from Run 4.A loud ‘pop’ noise was heard during the large pulse of Run 6, when one SMA bar was suspected to have ruptured in tension at the north side. Then, a similar noise was heard during Run 7, this time followed by a series of loud squeaking sounds that were synchronized with the motion of the column and were believed to be due to friction of the broken SMA bar ends sliding inside the ECC. High-definition cameras placed close to the plastic hinge region indicated that the crack at the north side opened significantly at the

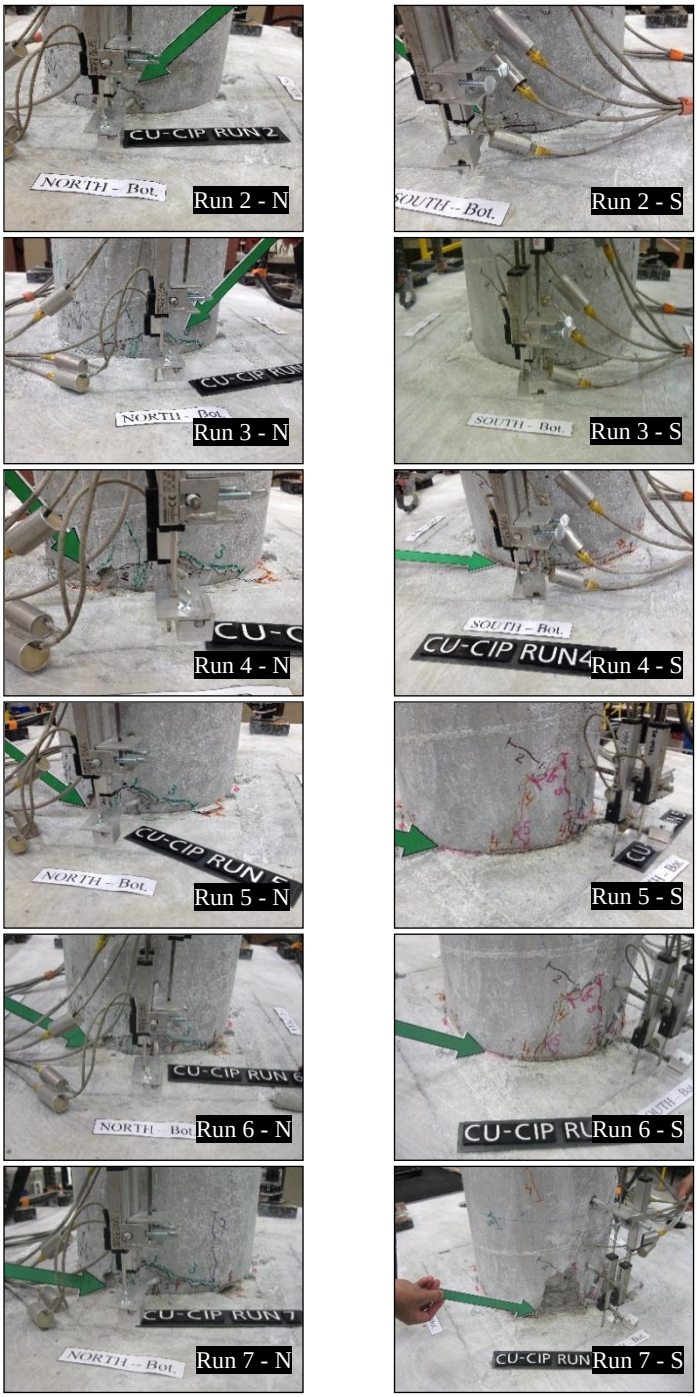

Figure 14. Damage state at the north and south sides after Runs 2 through 7.

instant of maximum force during Runs 6 and 7 (*Fig. 15*), when dust came out of the crack and the SMA bars ruptured. The crack subsequently closed due to the superelastic property of SMA. No major cracks or spalling were seen in the concrete section above the ECC at any time.

Figure 15. Tensile crack opening at the instant of maximum force during Runs 6 (left) and 7 (right).

Once the tests were concluded, the cover ECC was removed in order to expose and identify the broken SMA bars and rule out any misbehavior of the threaded connections. It was found that in effect two SMA bars ruptured in a ductile manner at the dog-bone segment on the north side (*Fig. 16*), and no failure of the threaded couplers occurred.

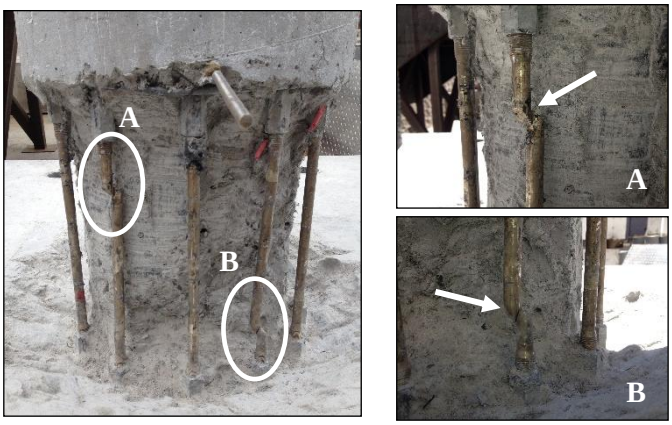

Figure 16. Broken SMA bars on the north side after cover removal.

3.3 Variation of fundamental period

White noise motions having frequency content from 0.5 Hz to 20 Hz, root mean square (RMS) acceleration of 0.012g, and duration of approximately 70 s were applied in between earthquake runs to monitor changes in the natural vibration period of the model arising from damage progression. Natural frequencies and periods were determined based on the lowest frequency peak in the transfer function between the Fourier spectra from the acceleration at the shake table level and the acceleration at the top of the column. The initial measured period

of the column model corresponding to the uncracked state was 0.379 s and increased progressively up to 0.531 s after Run 6, as the stiffness of the model degraded after each run. The vibration periods measured after runs 1 to 6 as a function of the PGA during each run are illustrated in *Fig. 17*, where a nearly linear correlation between the two can be seen. Since the period of CuAlMn SMA-ECC columns will be typically in the range of the descending branch of the response spectrum for motions recorded on stiff soil (see *Fig. 13*) and it will continue lengthening due to cumulative nonlinearity, the behavior of these columns under near-fault and intermediate motions could be potentially different than that of conventional concrete columns.

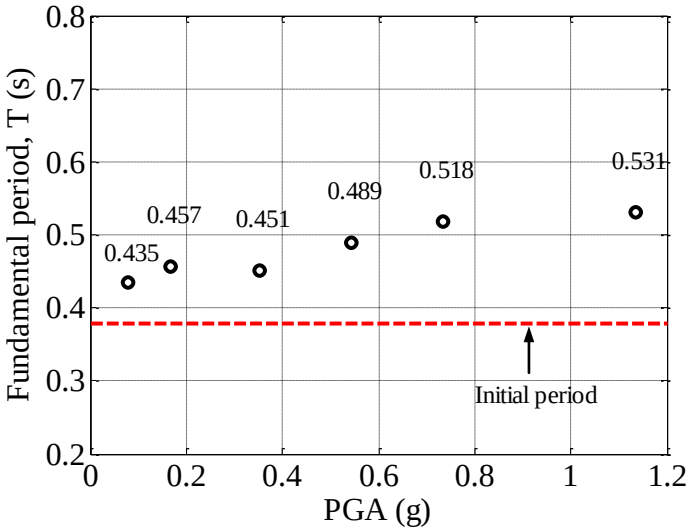

Figure 17. Lengthening of fundamental period as a function of PGA.

3.4 Hysteretic behavior, maximum force and drift demands and residual drifts

The cumulative hysteretic behavior of the column model along with the maximum force demands and their corresponding displacements for each run are shown in *Fig. 18*. Shown in this Figure is also the envelope in the dominant direction (top-right) with stars indicating the instant where rupture of the SMA bars occurred and a bi-linear idealization of the envelope curve, in which failure was assumed to occur at the first bar rupture. The results are also summarized in Table 5, where the maximum positive, negative and residual drifts are listed along with the energy dissipated (E_d), the chord stiffness (K_{chord}), the displacement ductility demand (μ_Δ) and the inelasticity index (*II*) in the dominant direction measured during each run.

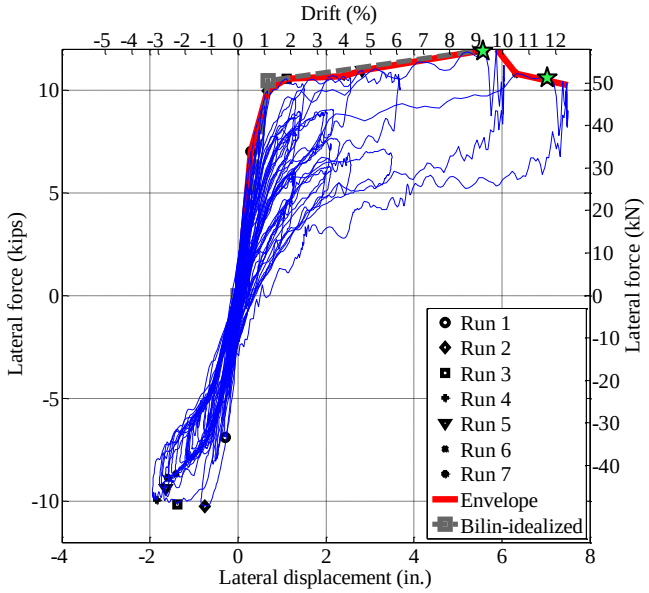

Figure 18. Hysteresis of the model tested.

*Table 5.*Summary of measured drift demands and hysteretic parameters.

Run #	Max. Drift +	Max. Drift -	Res. Drift	E_d (kips-in)	K_{chord} (kips/in)	μ_Δ^+	II^+
1	0.48%	-0.49%	0.01%	3.1	24.1	0.5	<0
2	1.06%	-1.33%	0.03%	13.9	14.2	1.0	<0
3	2.39%	-2.66%	0.02%	16.1	8.3	2.2	0.16
4	4.03%	-3.07%	0.04%	29.7	4.9	3.7	0.36
5	5.80%	-2.82%	0.08%	44.2	4.5	5.4	0.58
6	9.53%	-2.23%	0.22%	53.2	2.8	8.9	>1
7	11.80%	-2.71%	0.39%	66.7	2.1	11.0	>1

The inelasticity index (*II*) is a measure of the plastic displacement demand relative to the total plastic displacement capacity of the column and is defined as shown in Eq.(1). The maximum *II* is 1 and corresponds to failure, while an *II* of zero indicates the column displacement and force are at the effective yield point and a negative *II* indicates the column is elastic.

$$II = \frac{\Delta_{max} - \Delta_y}{\Delta_u - \Delta_y} \qquad (1)$$

where: Δ_{max} is the maximum displacement,
Δ_y is the effective yield displacement, and
Δ_u is the ultimate displacement.

The effective yield force, effective yield displacement and displacement ductility capacity of the column based on the bi-linear idealization were 10.47 kips (46.6 kN), 0.683 in. (17.35 mm) [1.1% drift], and 8.6, respectively, while the ultimate force and displacement were 12.06 kips (53.6 kN) and 5.868 in. (149.06 mm) [9.2% drift], respectively.

As seen in *Fig. 18*, the model did not experience a significant drop in lateral load capacity despite suffering rupture of 2 SMA bars while reaching maximum drifts of 9.5% and about 12% during Runs 6 and 7, respectively, and being subjected to ductility demands exceeding 5. Values for the inelasticity index indicate that the testing protocol was successful in pushing the column model to a wide range of plastic displacement demands and ultimately to its limit. Table 5 and *Fig. 17* show that there was substantial stiffness degradation due to yielding of longitudinal reinforcement despite the low apparent damage observed in *Fig.14*. The self-centering ability of the column was remarkable, as its residual drift was less than 0.5% even after having been subjected to a motion equivalent to 450% of the design earthquake and that it had a relatively low longitudinal SMA ratio. The level of energy dissipation the model exhibited was under-predicted by pre-test analytical studies, suggesting that additional sources of energy dissipation are present in Cu-SMA reinforced columns, in spite of using CuAlMn SMA bars with a very narrow hysteretic flag shape stress-strain relationship (see *Fig. 5*).

3.5 Measured strains and curvatures

3.5.1 Strains

A total of 44 strain gauges were installed at different locations on the spiral transverse reinforcement, the longitudinal mild steel, and the SMA bars. Most gauges were located inside the potential plastic hinge region, but some were placed above and below to monitor spread of plasticity to the mild steel. The gauges were rated to measure compressive and tensile strains up to 250,000 microstrain (με) or 25%. Several gauges placed in the longitudinal SMA bars ruptured or reached their working limit starting from Run 5. Strain gauge data and observations revealed that none of the spiral wires in the column yielded or ruptured during testing, as the maximum tensile strain recorded in the transverse reinforcement was -670 με (33% of yield). Strain profiles along the extreme bars on the north and south sides of the column are shown in *Fig. 19* and *Fig.20*. For clarity, *Fig. 19* shows the maximum compressive and tensile strains recorded during Runs 1-5 and *Fig. 20* shows those recorded during the last 2 runs, when some gauges were rendered inoperative.

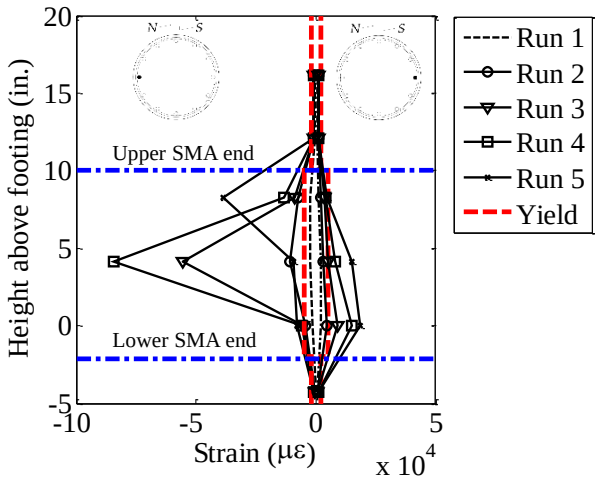

Figure 19. Strain profile along north and south for Runs 1 to 5 (Note: 1% strain=10,000 με).

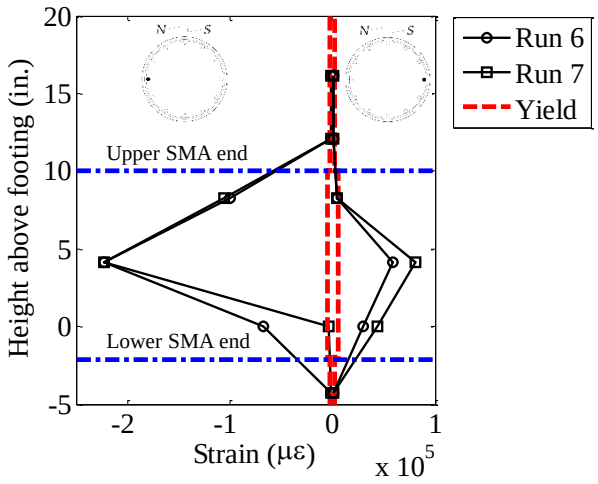

Figure 20. Strain profile along north and south for Runs 6 and 7 (Note: 1% strain=10,000 με).

Fig.19 and *Fig. 20* show that strains in the mild steel reinforcing bars above and below the plastic hinge stayed well below yield during all runs. Consequently, all nonlinear behavior took place in the plastic hinge region as intended and thus, the following discussion deals with the observed strains in the SMA bars only. The tensile strains in the north side (negative) were below yield during Run 1 and increased above yield starting from Run 2 up to Run 5, when they slightly decreased possibly due to localized damage. Tensile strains at the north increased again during Runs 6 and 7 until the limit of the strain gauges was reached. The last reliable reading from a strain gauge that was placed on the bar

that ruptured during Run 6 (see *Fig. 16*) show that the strain in the vicinity of the breaking location was about 180,000 με (18%), which exceeds the rupture strain of 14% that was measured during slow cyclic testing of a SMA bar specimen (*Fig. 5*). It is believed that this could be due to strain rate effects experienced by the SMA bars under near-fault motions as well as differences in the material and mechanical properties from different lots, as development of superelastic CuAlMn SMA is still work in progress. On the other hand, compressive strains on the south side (positive) were comparatively low up to Run 5, when a strain of 20,000 με (2%) was measured. These strains kept increasing during runs 6 and 7, and a maximum compressive strain in the SMA of about 81,000 με (8%) was measured during Run 7, showing the effectiveness of ECC and the spiral wire in restraining buckling of the SMA bars.

3.5.2 Curvatures and plastic hinge length

Several Novotechnik TR series displacement transducers were installed at the bottom north and south sides of the column to measure uplift, rotations and curvatures. The curvature was calculated by computing the slope of the strain profile of the column over the gage length. The average strains at each side of the column were calculated as the relative vertical displacements measured between any two points at one side divided by the gage length. Curvature profiles of the column model at the instants when maximum and minimum lateral forces occurred are shown in *Fig. 21*, where positive curvatures indicate displacements towards the dominant direction (south).

It can be seen that curvatures were linear and below yield above the SMA level, suggesting again that all nonlinear behavior took place in the region with SMA. Furthermore, the curvatures seemingly were unaffected by the boundary where ECC ended at 21 in. (533.4 mm) above the footing. In the dominant direction, curvatures increased linearly up to runs 4 and 5, when a region of approximately constant curvature was observed in the bottom half of the SMA region. Then, curvatures started increasing again in a nonlinear fashion during runs 6 and 7, possibly because some of the SMA bars in tension entered the strain hardening branch. The curvatures in the non-dominant direction were comparatively small but also displayed nonlinearity for all runs except for Run 1.

A region of approximately constant curvature was also observed at the bottom portion in the non-dominant direction during run 6, with a width of roughly half the SMA length or 5 in. (127 mm). This suggests the column also experienced nonlinear behavior in the non-dominant direction. Due to damage and large displacements at the zone where the steel rods holding the displacement transducers were attached to the column, curvature measurements during Run 7

in the non-dominant direction were erratic. Shown in *Fig. 21* are also the effective yield curvature (ϕ_{yield}) and the ultimate curvature ($\phi_{ultimate}$). The former was computed using the moment-area method with the effective measured yield displacement found in Section 3.4, while the latter was taken as the curvature measured at the instant where the first SMA bar ruptured during Run 6. From *Fig. 21* it is seen that curvatures during Run 1 were below yield, and then increased progressively above yield starting from the base of the column from one run to the next.

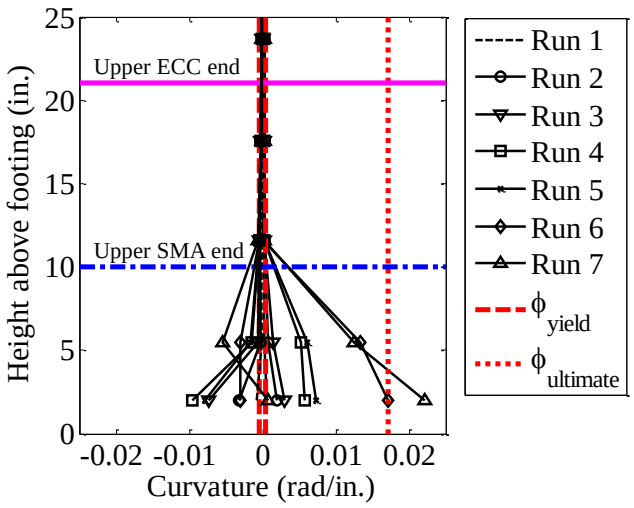

Figure 21. Curvature profiles at instants of maximum and minimum lateral force.

The plastic hinge length, L_p, of a concrete column is a very important parameter used to estimate the actual inelastic displacement and load carrying capacity during seismic evaluation and performance-based design of bridges. Plastic hinge regions are defined as those where substantial inelastic behavior takes place under extreme loading, such as in the base of the column in the present study. Nonlinear curvature distribution is typically assumed to be constant in these regions for ease of force and displacement calculations. Analytical derivation of a general expression for L_p is very complicated because this parameter is affected by several variables including member size, height, longitudinal reinforcement ratio and yield strength, and concrete compressive strength, and consequently a series of formulas based on experimental tests have been proposed by several researchers. Since there is no background on the inelastic behavior of columns with CuAlMn SMA and thus no methods exist to estimate their plastic hinge length, the applicability of several existing formulas originally developed for RC columns was studied. The “measured” plastic hinge

length in the present study was determined by solving Eq. (2) for L_p and was found to be equal to 5.13 in (130.3 mm), which is roughly one-half of the SMA length above the footing and is consistent with earlier discussions related to *Fig. 21*.

$$\Delta_p = \left(\phi_u - \phi_y\right) \cdot L_p \cdot \left(L - \frac{L_p}{2}\right) \qquad (2)$$

where: Δ_p is the plastic displacement (Δ_u- Δ_y) = 5.185 in. (131.7 mm),
Δ_y is the effective yield displacement = 0.683 in. (17.3 mm),
Δ_u is the ultimate displacement = 5.868 in. (149 mm),
ϕ_y is the effective yield curvature = 5.081 x 10^{-4} rad/in.,
ϕ_u is the ultimate curvature = 0.017084 rad/in., and
L is the length of the column = 63.5 in. (1612.9 mm).

A summary of the estimated plastic hinge length by various expressions existing in the literature and their respective error in comparison with the experimental value is shown in Table 6. The formula by Paulay and Priestley [16], currently used in the AASTHO Seismic Bridge Design Specifications [4] seems to better estimate the measured plastic hinge length (within 10%). Other expressions either overestimate or underestimate the actual plastic hinge length, including the equation by Mortezaei and Ronagh [21] that specifically takes into account the effect of directivity pulses under near-fault earthquakes.

*Table 6.*Calculated plastic hinge length by various methods.

	Ref.						
Ref.	[16]	[17]	[18]	[19]	[20]	[21] Near Fault	[22]
L_p (in.)	5.60	6.70	7.78	4.17	3.50	6.30	7.00
Error	9.2%	30.6%	51.7%	-18.7%	-31.8%	22.8%	36.5%

4 ANALYTICAL STUDIES

4.1 Post-test analyses

Finite element computer program OpenSees was used to create a 2-dimensional fiber model of the test column and perform a series of nonlinear dynamic analyses to estimate its response and evaluate the suitability of computer modeling methods. The achieved ground motions of the experimental program were used as input excitation at the base of the model, and were applied incrementally with constant axial load in order to accurately simulate the testing protocol. The most important features of the analytical model including the element types, section types and uniaxial material models that were used are

summarized in *Fig. 22*. Nonlinear beam column elements with distributed plasticity were used for both the ECC-SMA portion at the base of the column and the reinforced concrete section above it. Although test data showed that nonlinear behavior took place in the portion with SMA only suggesting an elastic element could have been sufficient to model the conventional RC portion above, it was found that using a fiber section-nonlinear element was necessary to accurately represent the stiffness of the column since reinforced concrete members crack even under low stress levels.

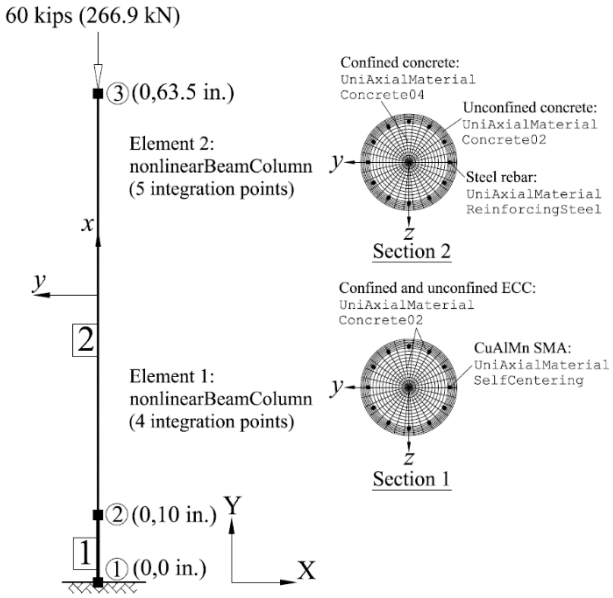

Figure 22. 2-D analytical model of the column inOpenSees.

The model by Motaref et al. [23] was used for the stress-strain behavior of confined ECC, while confined concrete was modeled per the modified Mander's model. Unconfined ECC and concrete were modeled using an adaptation of the Kent-Scott-Park model (Concrete02) with zero tensile strength. Steel reinforcing was modeled using the uniaxial material model by Chang and Mander [24], while the flag-shaped material model by Christopoulos et al. [25] was used for CuAlMn SMA. Stiffness-proportional Rayleigh damping was used by assigning a specific damping ratio to the fundamental vibration mode. Initial analyses demonstrated that using a customary damping ratio (2%) and a β factor of 0.20 for the SMA (see Table 2) did not result in a good match between the analytical and experimental results, since the test model exhibited higher damping and energy dissipation. Thus, a β factor of 0.50 and a damping ratio of 10% were necessary for the analytical model to closely match the experimental results. The results are summarized in *Fig. 23*, *Fig. 24*, and *Fig. 25*, where the analytical and experimental displacements, forces, and

hysteresis plots are shown, respectively. The maximum error between selected estimated and measured response parameters are listed in Table 7.

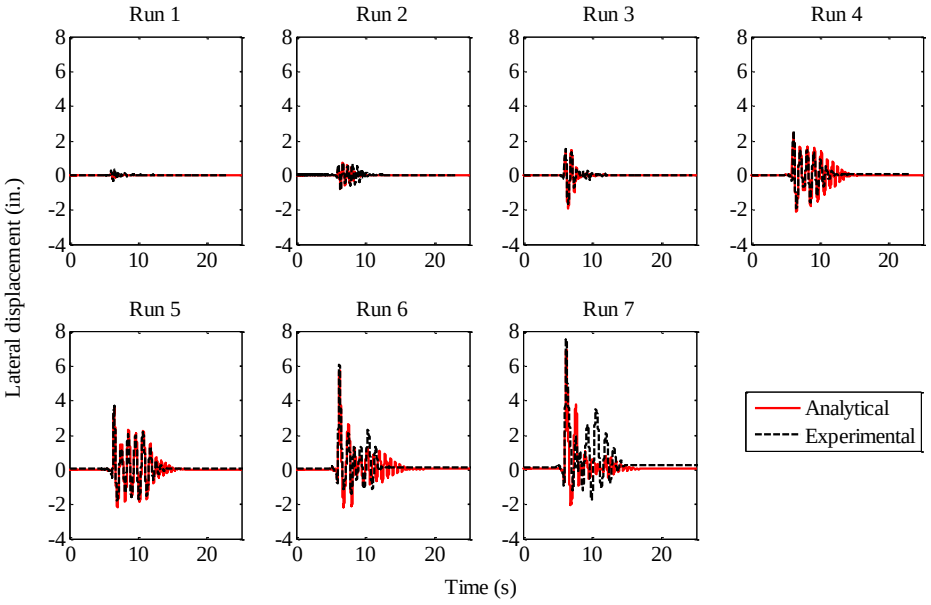

Figure 23. Comparison of analytical (OpenSees) and experimental displacements.

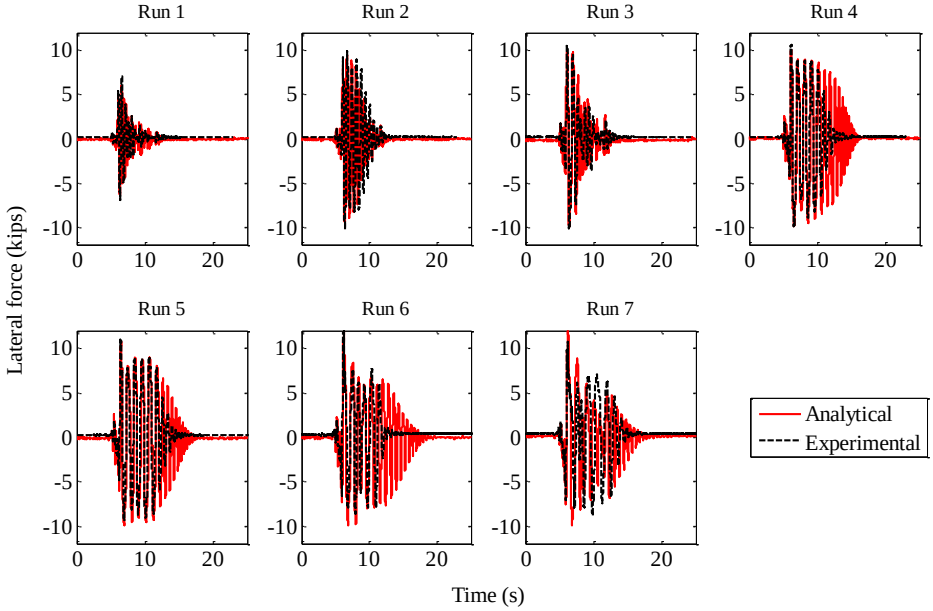

Figure 24. Comparison of analytical (OpenSees) and experimental forces.

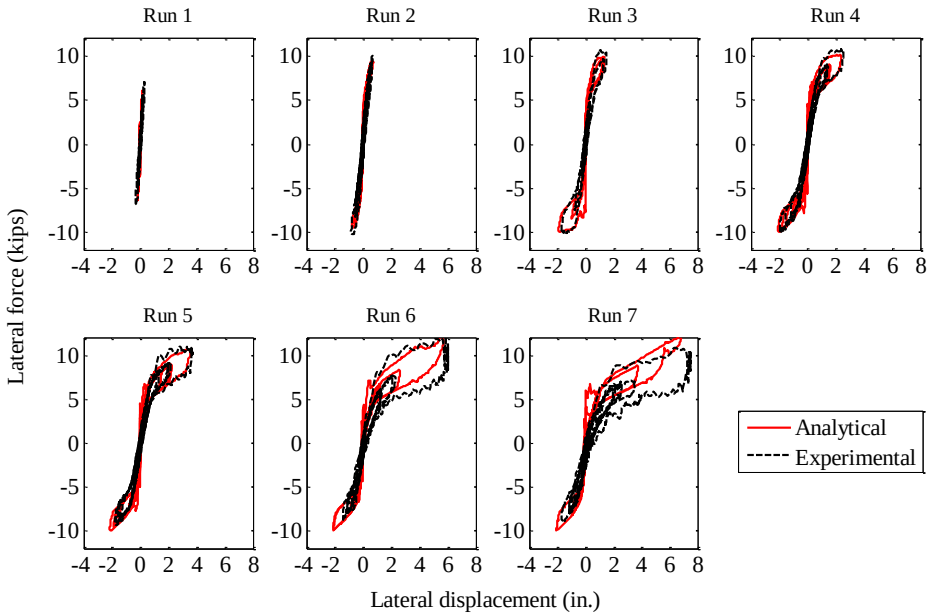

Figure 25. Comparison of analytical (OpenSees) and experimental hysteresis curves.

Table 7. Percent errors between selected analytical and experimental response parameters.

	Error			
Run #	Max. disp.	Max. force	Res. Drift	E_d
1	-41.2%	-13.7%	-103.8%	-69.9%
2	9.3%	-5.6%	-101.2%	-51.7%
3	-7.3%	-7.0%	-119.3%	25.9%
4	-5.6%	-5.9%	-91.7%	7.8%
5	-2.0%	-2.1%	-73.6%	3.0%
6	-5.8%	35.0%	-76.3%	0.2%
7	-8.0%	12.8%	-81.1%	-6.5%

The analytical model was able to accurately estimate the experimental results for the most part, but was unable to capture the high damping level that was observed in the lateral force towards the end of Runs 4 to 7. From *Fig. 23* and Table 7 it is seen that the maximum displacement in the dominant direction was accurately matched by the analysis (within a 10%) except during Run 1, when it was underestimated. The maximum lateral force estimations were good except

for Run 6, since the analytical model was not able to capture the SMA bar rupture that occurred during the test. The hysteresis behavior shown in *Fig. 25* was adequately represented by the analytical model, but SMA bar ruptures and high hysteretic damping that took place during Runs 6 and 7 caused some differences between the analytical and experimental results to be noted. Poor correlation was seen between the measured and analytical residual drifts, possibly due to the fact that experimental residual drifts were very low during all runs. With the exception of Runs 1 to 3, the analytical model was able to accurately match the cumulative energy dissipated during each run. The analytical results suggest that improvements are necessary in modeling to capture SMA bar fracture, modeling of damping, and estimating residual displacements.

4.2 Practical implications and differences with respect to conventional RC columns

Experimental and analytical results indicate that the seismic behavior of bridge columns with superelastic CuAlMn SMA and ECC would be potentially different than that of conventional steel-reinforced concrete columns. Since CuAlMn SMA has lower yield strength and elastic modulus than mild steel, these columns would be softer and weaker in comparison to their conventional RC counterparts. Furthermore, use of ECC in the plastic hinge region would additionally reduce column stiffness due to the lower modulus of elasticity of ECC caused by its lack of coarse aggregates. Consequently, designing CuAlMn-ECC columns to have comparable stiffness and lateral load capacity to those of conventional concrete columns would result in higher longitudinal reinforcement ratios that could lead to potential congestion and constructive issues unless a larger cross section is used. In addition, columns reinforced with CuAlMn SMA exhibit substantially lower energy dissipation compared to RC members. In this sense, the design philosophy for columns with CuAlMn SMA and ECC would need to be conducted under a displacement-based framework rather than a force-based approach. This is typically done in the field of seismic isolation, where flexibility is taken advantage of in order to lengthen the period of the structure to a region of lower spectral ordinates (and consequently lower seismic forces), while the structure experiences higher displacements. In such case, it would be necessary to design these innovative SMA-ECC columns for a controlled displacement under the design earthquake scenario and to detail them so that they can maintain their load-carrying capacity under a given design displacement. Conventional RC columns are designed to dissipate energy through plastic behavior because designing them to stay elastic is cost prohibitive and because softening arising from plastic behavior is desirable in order to limit the magnitude of the forces transmitted to capacity-protected elements. These same features essentially exist in CuAlMn SMA-ECC columns

with the added substantial advantage that they experience minimal or no damage and do not necessitate bridge closure after earthquakes.

5 CONCLUSIONS

Based on the analytical and experimental results of this study, the following conclusions can be drawn:

1. For the first time a bridge column using Copper-based superelastic SMA bars in the plastic hinge region was tested under near-fault ground motions. The column model exhibited a very high self-centering capability by having a residual drift of less than 0.5% even after being subjected to a maximum drift of around 12%.
2. Superelastic CuAlMn SMA and ECC that were used in the plastic hinge of the column substantially reduced the extent of apparent damage after subjecting the column to a motion equivalent to 450% the design earthquake.
3. Observed damage such as rupture of the SMA bars which occurred at approximately 18% tensile strain and minor spalling of the ECC cover did not significantly reduce the lateral and vertical load-carrying capacity of the column.
4. All of the nonlinear behavior of the model tested took place along the length in which SMA bars extended above the footing. No yielding or distress was noticed in the mild steel reinforcement, concrete, and ECC located above and below the SMA.
5. The measured plastic hinge length was about one half of the SMA length above the footing. This length was better estimated by the equation by Paulay and Priestley, currently adopted in the AASHTO Seismic Bridge Design Specifications.
6. A simple 2-dimensional analytical fiber model of the column tested that was developed in OpenSees was able to accurately estimate some of the key test results. This model will allow future analytical studies to be conducted in order to better understand the seismic behavior of bridge columns with SMA and ECC, although further refinement of the modeling method is warranted.
7. Using superelastic SMA and ECC in the plastic hinge regions of bridge columns located in regions of high seismicity could be a feasible alternative to keep bridges functional after strong earthquakes.

ACKNOWLEDGMENTS

Special gratitude goes to Dr. Sara Nerlove, the NSF Program Director for the Partnership for Innovation program, for her support and guidance. Furukawa Techno Material Co. of Japan is thanked for generously donating Copper-based SMA bars. Dr. Yoshikazu Araki of Kyoto University in Japan is thanked for his

technical input. Thanks are due Mr. Aaron Holmes at the NDOT materials lab for help with rebar testing. The continued assistance and help from staff members at the Earthquake Engineering lab at the University of Nevada, Reno is gratefully acknowledged. Visiting Researcher Kshitij Shrestha and graduate student Mehrdad Mehraein are thanked for their help during testing.

The material in this paper is based upon work supported by the National Science Foundation under Grant No. IIP-1114406. The UNR shake table site operation and maintenance is funded by Grant No. CMS-0402490.

REFERENCES

[1] EQE International, *The January 17, 1994 Northridge, California Earthquake, an EQE Summary Report*, San Francisco, CA, 1994.
[2] EQE International, *The January 17, 1995Kobe Earthquake, an EQE Summary Report*, San Francisco, CA, 1995.
[3] Earthquake Engineering Research Center, *Seismological and engineering aspects of the 1995 Hyogoken-Nanbu (Kobe) earthquake*, Report No. UCB/EERC-95/10, University of California, Berkeley, 1995.
[4] AASHTO, *AASHTO Guide Specifications for LRFD Seismic Bridge Design*, American Association of State Highway and Transportation Officials, Washington, DC, 2011.
[5] Fischer, G., and Li, V.C. "Effect of matrix ductility on deformation behavior of steel-reinforced ECC flexural members under reversed cyclic loading conditions"; ACI Structural Journal, Vol. 99 No. 6, pp.781-790, 2002.
[6] DesRoches, R., McCormick, J., and Delemont, M., "Cyclic properties of superelastic shape memory alloy wires and bars", ASCE Journal of Structural Engineering, Vol. 130 No. 1, pp. 38-46, 2004.
[7] Saiidi, M., and Wang, H., "An exploratory study of seismic response of concrete columns with shape memory alloys reinforcement"; ACI Structural Journal, Vol. 103 No. 3, pp.436-443, 2006.
[8] Saiidi, M., O'Brien, M., and Zadeh, M., "Cyclic response of concrete bridge columns using superelastic nitinol and bendable concrete"; ACI Structural Journal, Vol. 106 No. 1, pp.69-77, 2009.
[9] Cruz-Noguez, C., and Saiidi, M., "Performance of advanced materials during earthquake loading tests of a bridge system", ASCE Journal of Structural Engineering, Vol. 139 No. 1, pp. 144-154, 2013.
[10] Araki, Y., Endo, T., Omori, T., Sutou, Y., Koetaka, Y., Kainuma, R., and Ishida, K., "Potential of superelastic Cu-Al-Mn alloy bars for seismic applications", Earthquake Engineering and Structural Dynamics, Vol. 40, No. 1, pp.107-115, 2011.
[11] Shrestha, K., Araki, Y., Nagae, T., Omori, T., Sutou, Y., Kainuma, R., and Ishida, K, "Effectiveness of superelastic bars for seismic rehabilitation of clay-unit masonry walls", Earthquake Engineering and Structural Dynamics, Vol. 45, No. 2, pp.725-741, 2012.
[12] Shrestha, K., Araki, Y., Nagae, T., Koetaka, Y., Suzuki, Y., Omori, T., Sutou, Y., Kainuma, R., and Ishida, K., "Feasibility of Cu–Al–Mn superelastic alloy bars as reinforcement elements in concrete beams", Smart Materials and Structures, Vol. 22, No.2, 025025, 2013.
[13] Araki, Y., Maekawa, N., Shrestha, K. C., Yamakawa, M., Koetaka, Y., Omori, T., andKainuma, R., "Feasibility of tension braces using Cu–Al–Mn superelastic alloy bars", Structural Control and Health Monitoring, 2014.
[14] Gencturk, B., Araki, Y., Kusama, T., Omori, T., Kainuma, R., and Medina, F., "Loading rate and temperature dependency of superelastic Cu–Al–Mn alloys", Construction and Building Materials, Vol. 53, pp. 555-560, 2014.

[15] Phan, V., Saiidi, M., Anderson, J., and Ghasemi, H., "Near-fault ground motion effects on reinforced concrete bridge columns", ASCE Journal of Structural Engineering, Vol. 133, No. 7, pp. 982-989, 2007.
[16] Park, R., Priestley, M., and Gill, W., "Ductility of square-confined concrete columns", ASCE Journal of the Structural Division, Vol. 108, No. ST4, pp. 929-950, 1982.
[17] Paulay, T., and Priestley, M., *Seismic design of reinforced concrete and masonry buildings*, John Wiley and Sons, New York, NY, 1992.
[18] Priestley, M. and Park, R., "Strength and ductility of concrete bridge columns under seismic loading", ACI Structural Journal, Vol. 84, No. 1, pp. 61-76, 1987.
[19] Berry, M., Lehman, D., and Lowes, L., "Lumped plasticity models for performance simulation of bridge columns", ACI Structural Journal, Vol. 105, No. 3, pp. 270-279, 2008.
[20] Bae, S., and Bayrak, O., "Plastic hinge length of reinforced concrete columns", ACI Structural Journal, Vol. 105, No, 3, pp. 290-300, 2008.
[21] Mortezaei, A., and Ronagh, H., "Plastic hinge length of reinforced concrete columns subjected to both far-fault and near-fault ground motions having forward directivity", The Structural Design of Tall and Special Buildings, Vol. 22, pp. 903-926, 2013.
[22] Japan Road Association, *Seismic design specifications for highway bridges*, International Institute of Seismology and Earthquake Engineering, Tokyo, Japan, 2002.
[23] Motaref, S., Saiidi, M., and Sanders, D. "Seismic response of bridge columns with energy dissipating joints", Center for Civil Engineering Earthquake Research, Department of Civil and Environmental Engineering, University of Nevada, Reno, Nevada, Report No. CCEER-11-01, 2011.
[24] Chang, G., and Mander, J., "Seismic energy based fatigue damage analysis of bridge columns: Part I- Evaluation of seismic capacity", NCEER Report 94-0006, State University at Buffalo, NY, 1994.
[25] Christopoulos, C., Tremblay, R., Kim, H., and Lacerte, M., "Self-Centering Energy Dissipative Bracing System for the Seismic Resistance of Structures: Development and Validation", ASCE Journal of Structural Engineering, Vol. 134, No.1, pp. 96-107, 2008.

Received: July 17, 2014 Accepted: Noe 24, 2014